JGR Oceans

RESEARCH ARTICLE

10.1029/2025JC022530

Wind-Driven Iron Supply by Ekman Buoyancy Flux Enhances Phytoplankton Bloom in the Antarctic Circumpolar Current

R. Mole[1], W. J. von Appen[1], H. Becker[1], F. A. Haumann[1,2], T. Kanzow[1,3], A. Piñango[4], J. Stimpfle[1], S. Trimborn[1], and E. F. Young[5]

[1]Alfred Wegner Institute, Helmholtz Centre for Polar and Marine Research, Bremerhaven, Germany, [2]Ludwig-Maximilians-Universität München, Munich, Germany, [3]University of Bremen, Bremen, Germany, [4]Laboratório de Estudo do Oceano e do Clima, Instituto de Oceanografia, Universidade Federal do Rio Grande, Rio Grande, Brazil, [5]British Antarctic Survey, Natural Environment Research Council, Cambridge, UK

Key Points:

- Wind-driven Ekman buoyancy flux (EBF) enhanced mixing at the base of the mixed layer and drove an iron supply to the surface of the Southern Ocean
- The iron supply supported an intense phytoplankton bloom 1,000 km downstream of South Georgia in the early growing season
- EBF influences bloom heterogeneity and modulates the biological carbon sink in the Southern Ocean

Correspondence to:

R. Mole,
ryan.mole@awi.de

Citation:

Mole, R., von Appen, W. J., Becker, H., Haumann, F. A., Kanzow, T., Piñango, A., et al. (2025). Wind-driven iron supply by Ekman buoyancy flux enhances phytoplankton bloom in the Antarctic Circumpolar Current. *Journal of Geophysical Research: Oceans*, *130*, e2025JC022530. https://doi.org/10.1029/2025JC022530

Received 7 APR 2025
Accepted 17 JUL 2025

Author Contributions:

Conceptualization: R. Mole, W. J. von Appen
Data curation: R. Mole, A. Piñango
Formal analysis: R. Mole, W. J. von Appen, A. Piñango, J. Stimpfle, S. Trimborn
Funding acquisition: W. J. von Appen, T. Kanzow
Investigation: R. Mole, W. J. von Appen, A. Piñango, J. Stimpfle, S. Trimborn
Methodology: R. Mole, W. J. von Appen, H. Becker, A. Piñango, J. Stimpfle, S. Trimborn
Software: R. Mole
Supervision: W. J. von Appen, T. Kanzow
Visualization: R. Mole, W. J. von Appen
Writing – original draft: R. Mole, A. Piñango, J. Stimpfle, S. Trimborn

Abstract The Southern Ocean today is a globally relevant sink for atmospheric carbon dioxide (CO_2), where the biological uptake of carbon through primary productivity is largely controlled by widespread iron (Fe) limitation. We analyze observations from a submesoscale-resolving cross-section of the Antarctic Circumpolar Current (ACC) obtained around one thousand kilometers downstream of South Georgia in the Atlantic sector during austral spring 2022. Vertically integrated chlorophyll peaked in a strong (~250 mgChl-a m^{-2}) phytoplankton bloom within the central portion of the jet associated with the Southern ACC Front. We infer that winds drove a northward Ekman transport of dense water across the front and that this destabilized the water column, leading to an Ekman Buoyancy Flux (EBF) and enhanced vertical mixing ($\sim 1 \times 10^{-2}$ m^2 s^{-1}) across the base of the mixed layer. Using in situ measurements of dissolved iron, we estimate a net flux to the bloom of up to 3 μmolFe $m^{-2}d^{-1}$ from a subsurface pool. This large flux can supply the same amount of Fe per unit area in one day as that supplied to the upstream Georgia Basin bloom through deep wintertime entrainment in 1 year. We calculate the bloom's daily Fe demand from in situ ^{55}Fe uptake measurements by phytoplankton and find it to be of a similar order of magnitude as the EBF-driven supply. We conclude that the bloom's strength and compact latitudinal extent are explained by EBF. Thus, EBF represents a previously understudied mechanism, which contributes to bloom patchiness and modulates biologically mediated CO_2 drawdown in the iron-limited Southern Ocean.

Plain Language Summary The Southern Ocean absorbs a significant amount of atmospheric carbon dioxide, but its productivity is often limited by iron availability. In this study, we analyzed data from a high-resolution survey across a number of strong oceanic fronts downstream of South Georgia during spring 2022 in the South Atlantic. We found a strong phytoplankton bloom where eastward winds pushed dense water across the fronts, creating instability, which increased mixing between the surface and deeper, iron-rich water. This resulted in a supply of iron to the bloom, which supported the bloom's intense growth. Our findings suggest that this wind-driven mixing is a key, previously overlooked process that shapes phytoplankton blooms and influences uptake of carbon dioxide in the Southern Ocean.

1. Introduction

The Southern Ocean is remote and challenging to study but plays an outsized role in the global climate system, responsible for 43% of the oceanic uptake of anthropogenic carbon and supporting up to 75% of marine primary production north of 30°S through the export of upwelled nutrients (Rintoul, 2018). Surface waters in the Southern Ocean have among the highest nitrate concentrations in the global ocean (Reagan et al., 2024), yet it is classed a high-nutrient low-chlorophyll (HNLC) zone due to generally low levels of productivity (Venables & Moore, 2010). In situ iron fertilization experiments have shown that growth is limited by iron (Fe) (Boyd et al., 2007; Martin et al., 1990), as an input of Fe leads to an immediate and strong increase of phytoplankton growth in the open waters of the Southern Ocean (Boyd et al., 2007; de Baar et al., 1995).

As a result, the seasonal cycle of ocean-to-atmosphere carbon flux in the Antarctic Circumpolar Current (ACC) is complex, with upwelling of deep, CO_2 rich water in wintertime, leading to the Southern Ocean acting as a source

Writing – review & editing: R. Mole, W. J. von Appen, F. A. Haumann, T. Kanzow, A. Piñango, J. Stimpfle, S. Trimborn, E. F. Young

of carbon (Gruber et al., 2019), while southward transport and cooling of subtropical water masses and biological growth in areas with Fe inputs (from upwelling, land, and atmospheric sources) turn the Southern Ocean into an atmospheric carbon sink (Bushinsky et al., 2019; Strass et al., 2002, 2017).

Numerous studies have examined Fe sources in the Southern Ocean, including dust deposition, iceberg drift, biological scavenging, hydrothermal activity, and shelf sediments (Boyd et al., 2012; de Jong et al., 2012; Graham et al., 2015). Fe-rich waters are also often found in deeper layers, which can be brought to the surface through several mechanisms including upwelling due to bathymetry (Sergi et al., 2020), mesoscale strain (Zhang et al., 2019), or local wind patterns (Moreau et al., 2023). Tagliabue et al. (2014) examined vertical supply routes and found that, in general, Southern Ocean blooms are largely supported by a pulse of Fe during deep wintertime entrainment, which is subsequently recycled in the mixed layer to support growth throughout the growing season. Background diapycnal mixing of Fe-rich waters into the surface provided only a minor supply.

Under appropriate conditions, vertical mixing can be enhanced above background levels and locally increase the supply of Fe (Ardyna et al., 2019). A modeling study by Nicholson et al. (2019) showed that summer storms can enhance vertical diffusion and deepen the mixed layer but that this accounted for only a minor intraseasonal supply of Fe to the surface. Where storms interacted with strong oceanic fronts, however, the enhancement of diffusion and Fe supply increased and strengthened primary production by 20% for several days.

Strong winds and strong currents along oceanic fronts are ubiquitous in the ACC and, as both typically flow eastward, their interaction and alignment are likely commonplace. Winds blowing down-front (aligned with the oceanic thermal wind, i.e., eastward along the major ACC fronts) can establish a cross-front transport of dense water over light. This process, known as the Ekman buoyancy flux (EBF), has been demonstrated to intensify horizontal gradients at the front and inhibit restratification (Thomas, 2005; Thomas & Lee, 2005; Thomas & Ferrari, 2008). A number of modeling studies have further revealed that EBF can enhance exchange processes across the base of the mixed layer; for instance, it has been demonstrated that EBF can deepen the surface mixing layer on the less dense side of fronts, increasing the entrainment of nutrient-rich pycnocline water and strengthening blooms (Whitt, Lévy, & Taylor, 2017; Whitt, Taylor, & Lévy, 2017). Additionally, further studies have found that sufficiently strong winds along the ACC resulted in increased ventilation (downward mixing of oxygen) below the surface layer (Bachman & Klocker, 2020; Klocker, 2018). It is therefore likely that EBF can provide a route for local vertical exchange of nutrients but, given the transient and small-scale nature of this process, it is difficult to observe in the field.

At several locations downstream of islands within the ACC, specifically South Georgia in the Atlantic sector and Crozet and Kerguelen in the Indian sector, Fe limitation is alleviated and strong phytoplankton blooms occur every year. These blooms are fertilized with Fe by the islands, predominantly from sedimentary sources, which can be picked up by strong currents and advected long distances (Graham et al., 2015; Robinson et al., 2016). This advection can maintain a subsurface Fe pool, which can be brought to the surface further downstream. The bloom downstream of South Georgia is the strongest in the Southern Ocean, estimated to be responsible for an annually averaged drawdown of 12.9 mmolC m^{-2} d^{-1} (Jones et al., 2012). Chlorophyll concentration typically peaks around 3 mg m^{-3}, and the bloom is relatively long-lived, lasting up to 200 days (Thomalla et al., 2023). Consequently, it has the largest annual Fe utilization of any bloom within the Southern Ocean (excluding the continental shelf off South America), estimated up to 60 μmolFe m^{-2} yr^{-1} (Boyd et al., 2012)—equivalent to a mean of 0.3 μmolFe m^{-2} d^{-1} over 200 days.

South Georgia lies on a shallow plateau with a mean depth ~200 m (Figure 1a). Fe advected form the shelf is likely to support the downstream bloom (Schlosser et al., 2018), which extends out of the Georgia Basin and has been linked to a subsurface Fe pool advected at least as far east as 20°W below the mixed layer (Venables & Meredith, 2009). Directly above the shelf, vertical exchange is expected to supply up to 0.41 μmolFe m^{-2} d^{-1} (Schlosser et al., 2018) but this falls below 0.01 μmolFe m^{-2} d^{-1} in the open waters of the Georgia Basin, predominantly supplied through deep wintertime entrainment (Tagliabue et al., 2014). For a region 1,250 km downstream of South Georgia, Schlosser et al. (2018) calculated that only a third of the estimated utilization of 0.33 μmolFe m^{-2} d^{-1} can be supplied from "new" (i.e., nonbiologically recycled) sources and that vertical mixing accounted for only a minor portion of this supply. Studies have concluded that efficient biological processes provide the shortfall of Fe (Borrione et al., 2014; Schlosser et al., 2018), or otherwise that there must be an unidentified persistent supply of Fe to the South Georgia bloom throughout the growing season (Korb et al., 2008; Nielsdóttir et al., 2012). Vertical supply of new Fe, however, is commonly calculated assuming vertical mixing

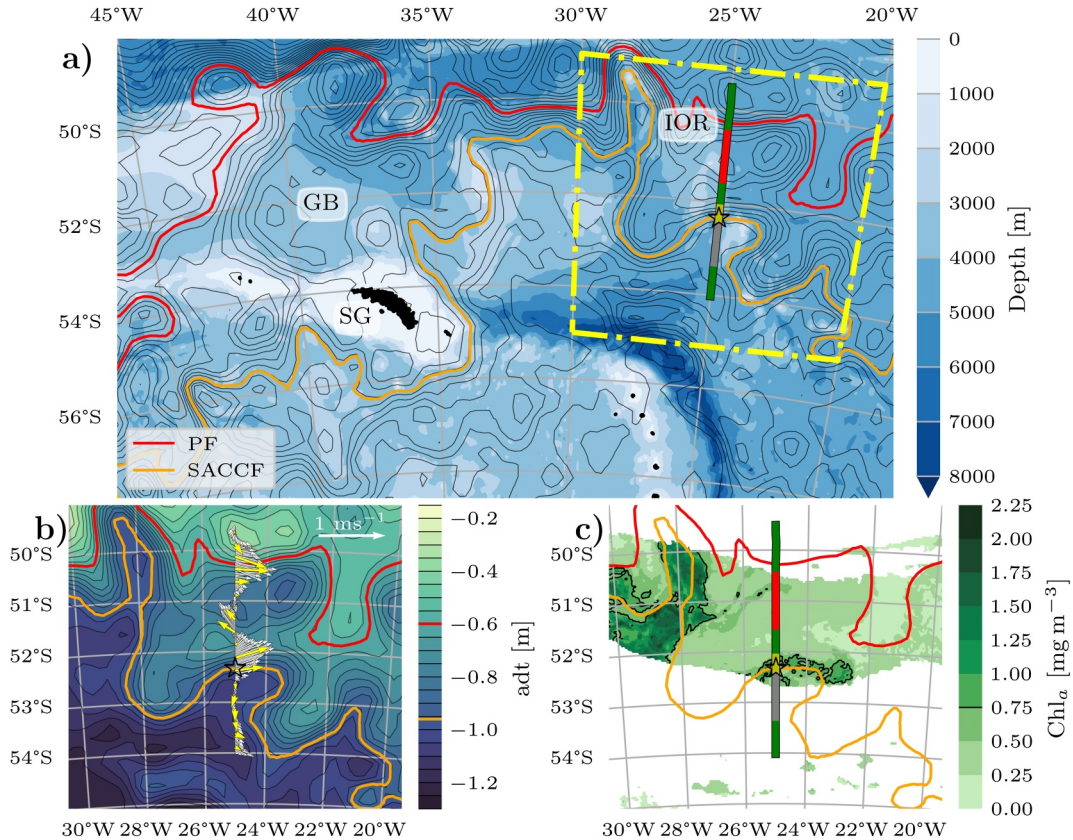

Figure 1. (a) Overview of the study area showing the transect along 25°W (green line) with the yellow box indicating the region of panels (b and c). Colored contours indicate the positions on 20 October 2022 of the polar front (red) and Southern Antarctic Circumpolar Current Front (orange), determined as described in the text. Black contours indicate absolute dynamic topography (ADT) with the same levels as in panel (b). Background shading indicates bathymetry. SG, South Georgia, GB, Georgia Basin, and IOR, Islas Orcadas Rise. Yellow and gray portions of the transect indicate the areas highlighted in subsequent figures while the red portion indicates the cyclonic structure crossed at 51°S. (b) ADT in the region indicated. Yellow arrows indicate the geostrophic velocities derived from the ADT data set, and gray arrows are the in situ velocities measured by the ship ADCP, averaged over the upper 50 m of the water column and smoothed to an approximate 2.6 km (≈ 0.025°) resolution. (c) Surface concentration of chlorophyll a on 22 October 2022 obtained from https://www.oceancolour.org (OC-CCI v6.0). The stars in all panels indicate the location of CTD station 6.

rates at low, background levels, which are typical for the open ocean but which necessarily exclude periods of enhanced vertical mixing and so underestimate the total vertical supply. As transient episodes of enhanced mixing can occur under atmospheric and oceanic conditions common in the ACC, such episodes may provide an additional input of Fe throughout the growing season.

In this study, we report on an open ocean transect in the region of the extended bloom (25°W), ~1,000 km downstream of South Georgia during early spring 2022. The transect crossed the main ACC fronts (SB: southern boundary, SACCF: Southern ACC front and PF: polar front), and we encountered spatially constrained high chlorophyll concentrations (i.e., above 0.75 mg m^{-3}) in a bloom across the SACCF. Our objective is to investigate this bloom, identify physical mechanisms that may enhance the supply of Fe to the surface, and evaluate the impact on local carbon uptake in the ACC. We show that enhanced vertical mixing, driven by the interaction of ACC fronts and local winds, may bring Fe to the surface in the wake of South Georgia and contribute significantly to the annual Fe supply to the bloom. Our findings contribute to the growing understanding of wind-driven biophysical coupling and shed light on a previously understudied Fe supply mechanism, which may enhance carbon uptake in Southern Ocean blooms.

2. Data

In situ data were collected as part of the GEOTRACES process study "Island Impact" using *RV Polarstern* (cruise PS133.1), which took place during early Austral spring (from 2 October to 17 November) 2022. We focus on data from a southward transect crossing several fronts of the ACC along 25°W and include biogeochemical parameters obtained using a trace metal clean CTD at station 6, near the center of the transect (Figure 1a). The transect began at 03:10 UTC on 19 October 2022 and covered approximately 500 km from 49.46°S to 54.02°S, ending at 15:10 UTC on 20 October 2022. A towed undulating profiler sampled the upper water column for the duration of the transect, while vessel-mounted instruments and laboratory-based systems measured surface water properties and velocities in the upper water column. Station 6 (52.33°S 24.96°W) began at 01:27 UTC on 22 October 2022.

2.1. Triaxus Data

We deployed a MacArtney Triaxus undulating system to follow a sawtooth pattern behind the vessel. The greatest flight depth that could consistently be achieved was 300 m, and the minimum depth of undulation was limited to 13 m, due to peak wave heights in excess of 9 m during the transect. With a vertical speed of ∼1 ms^{-1} and a horizontal speed of ∼4 ms^{-1}, the resulting horizontal resolution between consecutive upcasts was approximately ∼2.3 km. In total, 242 undulations were achieved along the transect.

The Triaxus was fitted with a SeaBird SBE 911plus CTD instrument configured with dual SBE3 temperature and SBE4 conductivity sensors, as well as an SBE43 dissolved oxygen sensor and a WETLabs WETStar environmental characterization optics (ECO) fluorometer. The single SBE43 dissolved oxygen sensor was precruise calibrated but otherwise not corrected or compared to other in-water sensors. Hence, we do not claim the absolute values are accurate but instead limit interpretation in this manuscript to identifying relative changes, which are not affected by absolute offsets, and so believe our statements are reliable. A Satlantic Deep SUNA nitrate sensor was also mounted to the platform and gathered data independent of the CTD system. The configuration during the cruise, including precruise calibration of sensors, is detailed here as follows: https://hdl.handle.net/10013/sensor.91419372-8cd2-4fa9-ae2e-a9f17451d3ff. All upcast data were processed following von Appen et al. (2020) onto a grid with a vertical spacing of 5 m and a horizontal spacing of 0.02°(∼2.2 km).

2.2. Vessel-Mounted ADCP Data

Vertical profiles of ocean velocity were obtained using a Teledyne RDI Ocean Surveyor 150 kHz acoustic doppler current profiler (vmADCP) mounted to the hull of *RV Polarstern*. Data from this instrument were processed using the Ocean Surveyor Sputum Interpreter (OSSI) software developed by GEOMAR and gathered into 4 m bins starting from 19 m depth. Data were further binned to 5 min (∼1.2 km) averages and, to satisfy the requirement of at least 90% good data, the deepest bin was at 287 m. Velocities were first interpolated onto the same grid as the Triaxus data where it was necessary to combine with density data (Figure 4b).

2.3. Underway and Thermosalinograph Data

Measurements of surface water properties were continually gathered using a thermosalinograph and autonomous FerryBox system (Petersen, 2014) during the transect. Measurements of fluorescence were made by the FerryBox, which was located slightly inside the hull; data were downloaded from the ship server with a time resolution of 5 s, and any gaps in the data were filled using a piecewise cubic Hermite polynomial (pchip) to preserve shape. The thermosalinograph measured temperature directly at the inlet on the hull of the ship and salinity a short way inside at the location of the instrument. Thermosalinograph data were downloaded at 1 min resolution (Hoppmann et al., 2023). All data were low-pass filtered by convolution with a 5-min wide Hanning window, resulting in an effective window size of approximately 1.2 km at a typical ship speed of 8 knots throughout the transect.

2.4. Sea Surface Height and Wind Data

We complement in situ data gathered during the campaign with satellite observations and derived quantities to place our findings in a wider spatial context. Daily values of sea surface height (SSH) and the derived meridional and zonal components of geostrophic velocity were obtained from the level-4 Global Ocean Gridded Sea Surface Heights and Derived Variables in the near-real time data set available from the E.U. Copernicus Marine Service (https://doi.org/10.48670/moi-00149). In addition, we obtained hourly values for wind stress at 0.125° resolution

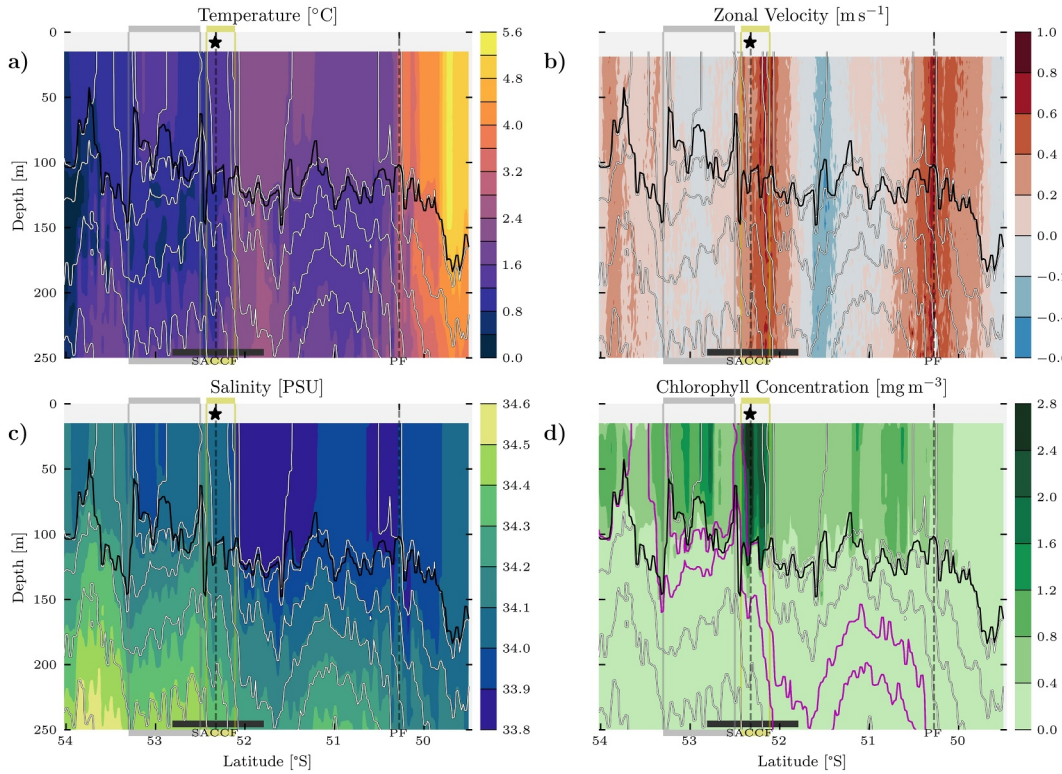

Figure 2. Sections of (a) potential temperature, (b) zonal (eastward) velocity, (c) salinity, and (d) chlorophyll concentration during the transect along 25°W. The magenta lines in panel (d) highlight the 1,027.30 and 1,027.38 kg m^{-3} isopycnals. In all panels, the black lines indicate the mixed layer depth (MLD); gray lines indicate isopycnals separated by 0.08 kg m^{-3}; dashed vertical lines indicate crossings of the Polar Front (PF) and Southern Antarctic Circumpolar Current Front (SACCF); the stars indicate the latitude of CTD station 6; thick horizontal black bar indicates the latitudinal range of Figures 4 and 5; colored boxes indicate areas which are also highlighted in Figure 1: (gray) where the transect was orientated downstream; and (yellow) the boundary of the bloom.

from the Global Ocean Hourly Sea Surface Wind and Stress from Scatterometer and Model data set also available from the E.U. Copernicus Marine Service (https://doi.org/10.48670/moi-00305).

2.5. Biogeochemical Parameters

At station 6, seawater was collected trace metal clean from 20 to 1,000 m depth applying GEOTRACES protocols (Cutter et al., 2017) and using a SeaBird SBE 911plus CTD system consisting of a titanium rosette equipped with 24 Model 114OC-12 12L bottles from Ocean Test Equipment. To minimize potential trace metal contamination, a metal-free winch system equipped with a synthetic reinforced Vectran cable was used. Each bottle was sampled directly in a clean laboratory container (ISO Class 5) equipped with several clean benches (ISO Class 3, MK Versuchsanlagen, Muecke-Merlau, Germany). Dissolved Fe concentrations were determined at AWI on a SeaFast system (Elemental Scientific, Omaha, NE, USA) coupled to an inductively coupled plasma mass spectrometer (ICP-MS, Element2, Thermo Fisher Scientific, resolution of R = 2,000), as described in Balaguer et al. (2023). Primary production and Fe uptake of the in situ phytoplankton community was determined at 20 m only. To this end, 3 µCi of ^{14}C-bicarbonate (Perkin Elmer, specific activity of 56.6 mCi mmol^{-1}) as well as ^{55}Fe (Perkin Elmer, specific activity of 325.11 mCi mg^{-1}, as $FeCl_3$ in 0.5 NHCl) were added to triplicate samples, giving a final concentration of 0.05 nM ^{55}Fe. After 24 hr in an on-deck incubator under ambient temperature and light conditions, the reaction was terminated and uptake rates of ^{14}C and ^{55}Fe were measured onboard on a liquid scintillation counter (Tri-Carb 2900 TR, Perkin Elmer). ^{14}C primary production and ^{55}Fe uptake rates were determined as described in Balaguer et al. (2023) and Böckmann et al. (2021), respectively.

2.6. CO_2 Fugacity and Fluxes

Surface underway continuous measurements of the seawater CO_2 molar fraction were carried out along the cruise with a General Oceanics 8050 pCO_2 Measuring System equipped with a spray-head equilibrator and a LICOR 7000 infrared gas analyzer. These measurements were calibrated using three standard gases ranging from 0 to 719 ppmv and then converted to wet CO_2 fugacity measurements (fCO_2) following the standard operating procedures described by Dickson et al. (2007), using data from the temperature and pressure sensor of the instrument and the sea surface temperature (SST) and salinity (SSS) values recorded using the thermosalinograph. Atmospheric CO_2 molar fraction measurements were carried out with the same instrument at a 2-hourly frequency. After calibration, these values were linearly interpolated and processed to obtain an atmospheric air CO_2 fugacity value for each seawater measurement. CO_2 fugacity (fCO_2) was used instead of the more common partial pressure of CO_2 (pCO_2) to take into account the nonideal behavior of gases and to provide a more accurate representation of the CO_2 content. To ensure an fCO_2 uncertainty below 2 µatm, only measurements where the difference between the sea surface and equilibrator temperature was less than 1°C were used. The CO_2 fluxes between the ocean and the atmosphere were calculated using the bulk flux equation $\mathcal{F}CO_2 = K_s K_t \Delta fCO_2$. Here, K_s corresponds to the CO_2 solubility coefficient of Weiss (1974) calculated from the SST and SSS data; K_t is the gas transfer velocity parametrization of Wanninkhof (2014) applied to the wind speed data measured by the weather station of the ship. ΔfCO_2 is the difference between the seawater and atmospheric CO_2 fugacity values and has virtually the same numeric value as the equivalent ΔpCO_2.

3. Derived Quantities

The transect from north to south along 25°W was approximately aligned with the cross-stream direction for most of the section (Figure 1b). Consequently, we maintain a geographical coordinate system, longitude x, and latitude y, throughout this paper. Velocities u (positive eastward) and v (positive northward) correspondingly approximate along- and across-stream flow. Regions where the mapping between stream and geographical coordinate systems diverges are highlighted by the gray box in Figures 2–5. In addition to the quantities outlined below, we also calculate apparent oxygen utilization as the 100% saturation concentration of oxygen (computed using `sw_satO2` from the Matlab SeaWater toolbox, available at http://www.cmar.csiro.au/datacentre/ext_docs/seawater.html) minus the measured oxygen concentration.

3.1. Dynamical Numbers

We calculate the latitudinal (approximately cross-front) buoyancy gradient $M^2 = \frac{\partial b}{\partial y}$, where the buoyancy $b = -\frac{g}{\rho_0}(\rho - \rho_0)$ and ρ_0 =1,025 kg m^{-3} is a nominal background density, and vertical stratification is $N^2 = \frac{\partial b}{\partial z} = -\frac{g}{\rho_0}\frac{\partial \rho}{\partial z}$ (z positive upward). We do not resolve structure in the along-front direction as we are limited to approximately cross-front transect data. Under the assumption that gradients along the front are much smaller than gradients across the front (i.e., $\frac{\partial}{\partial x} \ll \frac{\partial}{\partial y}$), we approximate relative vorticity as $\zeta = \frac{\partial v}{\partial x} - \frac{\partial u}{\partial y} \approx -\frac{\partial u}{\partial y}$. By normalizing the relative vorticity with the Coriolis frequency f, we get an estimate for the Rossby number $Ro \approx -\frac{1}{f}\frac{\partial u}{\partial y}$. We calculate mixed layer depth (MLD) along the transect using a density threshold method, defined as the interpolated depth where density exceeds the value in the uppermost cell by 0.05 kg m^{-3}.

3.2. Wind-Driven Ekman Processes

The surface of the ocean responds to sustained wind stress τ, by establishing an Ekman current, which decays away from the surface in the shape of a spiral. The vertically integrated transport of this current is oriented to the left of τ (in the Southern Hemisphere) and is largely confined above the Ekman depth (the shallowest depth at which the current opposes the direction of wind flow at the surface). Thomas and Ferrari (2008) give an approximate scaling for the thickness of the Ekman layer as follows:

$$H_e \sim (0.4/f)\sqrt{|\tau|/\rho}. \quad (1)$$

The lateral advection of water across fronts by Ekman transport modifies buoyancy within H_e. The differential transport of buoyancy at the front is balanced by a buoyancy flux extracted from the fluid below (Thomas, 2005; Thomas & Lee, 2005; Whitt, Lévy, & Taylor, 2017), termed the EBF and quantified by

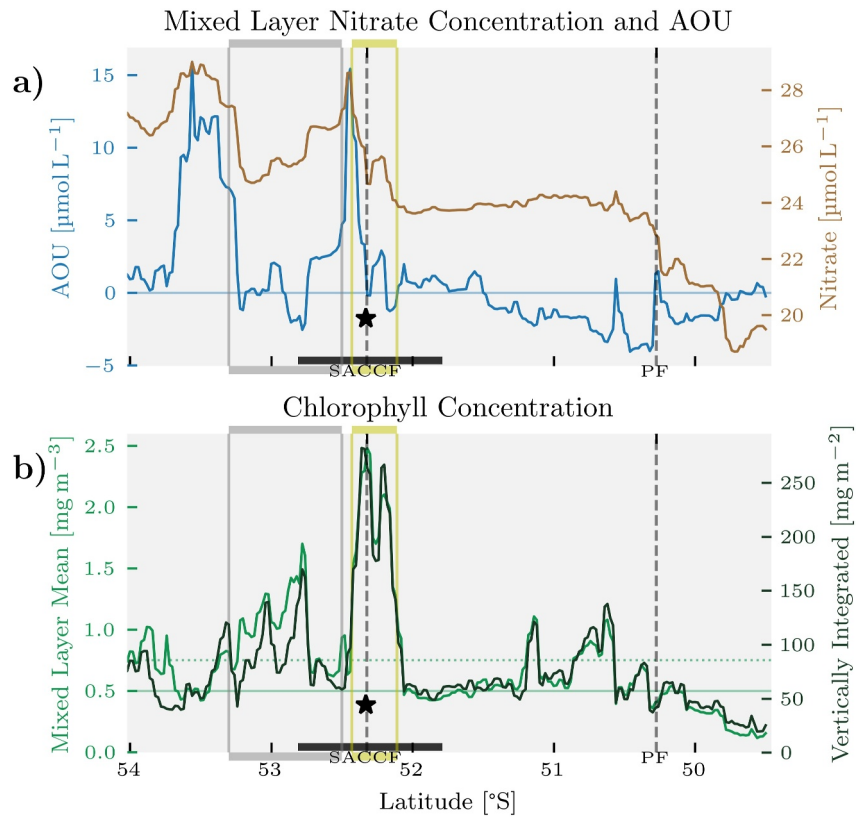

Figure 3. (a) Mixed layer mean values of nitrate concentration and apparent oxygen utilization during the transect along 25°W. (b) Mixed layer mean and vertically integrated chlorophyll concentration (calculated as the mixed layer mean value multiplied by the mixed layer depth). The horizontal dashed line indicates a mixed layer mean value of ∼0.75 mg m^{-3}. In both panels, the star indicates the approximate location of CTD station 6. Vertical dashed lines and colored boxes are as in Figure 2.

$$EBF = -\frac{\tau_x}{\rho f}\frac{db}{dy}. \tag{2}$$

This flux exits the deeper layer and acts to strengthen or weaken stratification below H_e. In the case of down-front winds (i.e., in the direction of the oceanic thermal wind), the horizontal transport reduces buoyancy within H_e resulting in a flux of positive buoyancy ($EBF > 0$) from below and weakening stratification. This process can destabilize the water column through gravitiational instability and has been shown in a modeling study by Whitt, Lévy, and Taylor (2017) to lead to both the enhancement of mixing at the base of the mixed layer, as well as its deepening into a subsurface nutricline.

EBF is extracted from below H_e and, for deep mixed layers ($MLD > H_e$), it is not clear how efficiently the flux is transmitted to the base of the mixed layer through instability-induced mixing, rather than changing the buoyancy of mixed layer below H_e. In this paper, we use EBF to estimate mixing at the base of the mixed layer driven by the reduction of buoyancy within H_e and assume a direct conversion between the two. Our estimates therefore represent an upper limit of the mixing, which could be induced within the upper water column by the Ekman advection of buoyancy across fronts.

4. Results

4.1. Regional Circulation

During the transect, three broad, eastward flowing jets were crossed. We defined the exact crossing of each front as the location of maximum horizontal surface density gradient and used this to obtain their associated sea surface height (SSH) values as follows: −0.60 m at 50.28°S, −0.84 m at 52.32°S, and −1.11 m at 53.92°S. At the time of

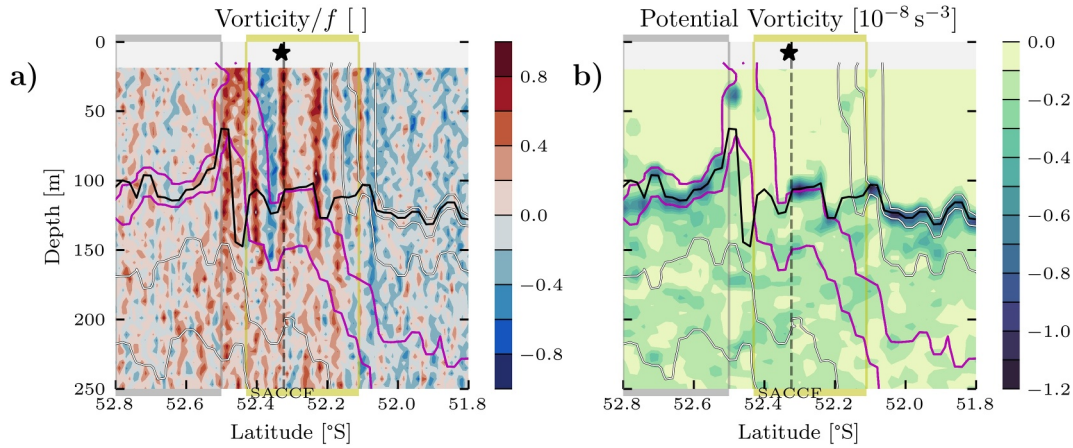

Figure 4. Sections plots around the bloom, represented by the solid black bar in previous figures. (a) Normalized relative vorticity (approximately Rossby number) and (b) potential vorticity. The frontal jet associated with the SACCF is approximately aligned with the yellow box (compare to Figure 5c). The vertical dashed line indicates the location of maximum surface density gradient in the SACCF. Black, gray, and magenta lines, as well as the colored boxes and stars are as described in Figure 2.

the transect (Figure 1a), contours for the first and second of these SSH values follow typical paths through the South Georgia region for the polar front (PF) and Southern ACC front (SACCF), respectively (e.g., Korb et al., 2004), so we adopt these labels. The PF enters the Georgia Basin from the west and circulates cyclonically around its northern edge while the SACCF loops anticyclonically around the South Georgia shelf before reflecting eastward. These fronts surround South Georgia and the Georgia Basin; hence, the portion of the transect between them is effectively downstream of the main bloom, which typically fills the Georgia Basin.

The zonal jets associated with these fronts appear to be barotropic (at least over the top 250 m, Figure 2b) and balanced by steeply sloped isopycnals, which separated distinct water masses with surface salinity increasing and temperatures decreasing toward the south (Figures 2a and 2c). In situ speeds peaked at ∼0.6 m s^{-1} in the PF and SACCF jets and agree well with altimetry-derived geostrophic velocities, both capturing a similar structure (Figure 1b). Velocities were largely oriented in an east-west direction for most of the transect, supporting our assumption that zonal gradients are likely to be much smaller than meridional (i.e., $\frac{\partial}{\partial x} \ll \frac{\partial}{\partial y}$). Between 52.5°S and 53.5°S, however, in situ and geostrophic velocities turn southward and run parallel to the transect. Our assumption breaks down in this region, which is marked by the gray box in Figures 2–5. This southward turn is driven by seafloor topography, which deflects the SACCF (roughly at 52.5°S, 24.5°W, Figure 1a), a location, which has the potential for Taylor column formation (Meredith et al., 2015).

The recent history of waters within the surface layer can be inferred from AOU (Figure 3a): values of AOU below zero (i.e., oxygen supersaturation) are typically indicative of sustained primary production whereas high values of AOU are indicative of the recent entrainment of water from deeper layers within timescales of ∼2 weeks, the equilibration time for oxygen at the surface. The AOU peaks south of the SACCF were coincident with similar peaks in nitrate concentration (Figure 3a), suggesting that the nitrate was recently sourced from entrained deep water. A particularly sharp AOU and nitrate peak at 52.4°S was colocated with steeply sloped, outcropping isopycnals at the southern edge of the SACCF (Figure 2), where AOU and nitrate concentrations reached up to 15.4 and 28.6 μmol L^{-1}, respectively. This feature (hereafter "the upwelling") was approximately 10 km across, and the high values of AOU confirm that the surface waters contained upwelled water of deep origin. The isopycnals associated with this upwelling (densities between approximately 1,027.30 and 1,027.38 kg m^{-3}, Figure 2) occupy depths between 100 and 150 m (i.e., the winter water depth range) to the south, but rapidly descend below 200 m within ∼45 km to the north of their outcropping.

4.2. Chlorophyll

Mean chlorophyll concentration within the mixed layer (ML) remained ∼0.5 mg m^{-3} throughout most of the study area south of the PF (Figures 2d and 3b), approximately 50 mg m^{-2} when integrated across the ML depth. In

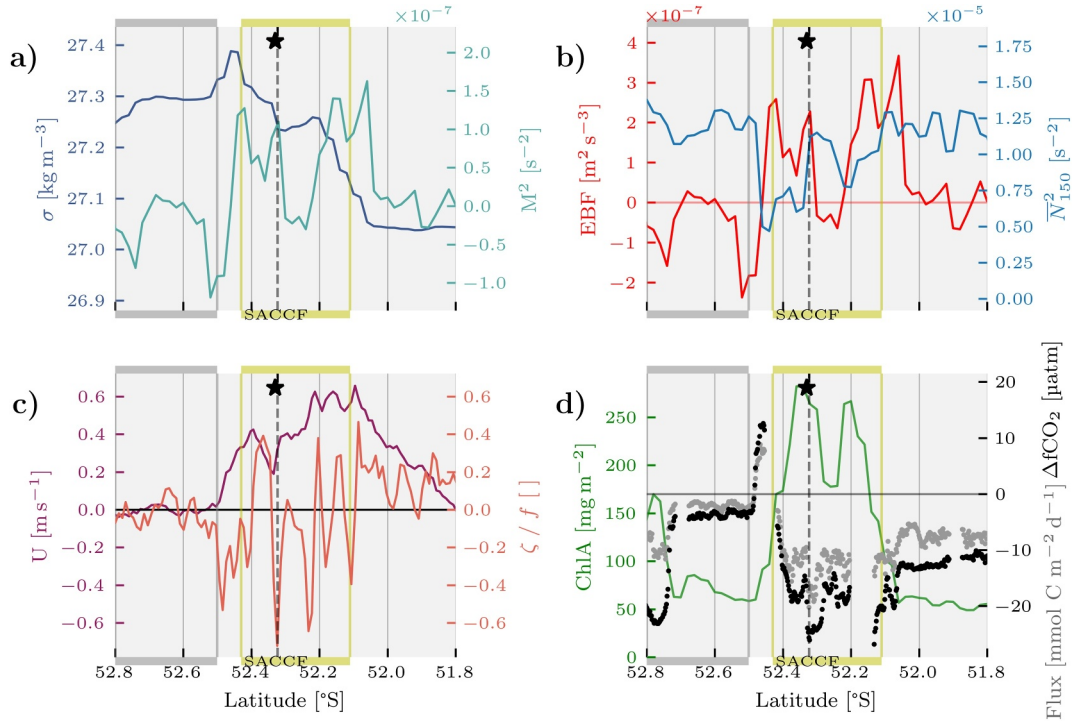

Figure 5. Mixed layer mean quantities across the same domain as Figure 4. (a) Density anomaly (σ) and horizontal buoyancy gradient (M^2). (b) Ekman Buoyancy Flux and mean stratification within the upper 150 m of the water column ($\overline{N^2}_{150}$). (c) Zonal velocity (U) and normalized relative vorticity (ζ / f). (d) Atmospheric CO_2 flux, ΔfCO_2, and vertically integrated chlorophyll (as in Figure 3). The gap near 52.2°S in CO_2 data is due to the 2-hourly self-calibration of the instrument. Vertical dashed lines, colored boxes, and stars are as in Figure 2.

a number of locations, however, the concentration rose above 0.75 mg m^{-3}, for example, near 51°S where chlorophyll concentration peaked at 1.11 mg m^{-3} (138 mg m^{-2}) during transit across a cyclonic structure (marked as the red portion of the transect in Figure 1a). Further south, a number of chlorophyll peaks occurred around 53°S (Figure 3b) at the center of a cyclonic meander of the SACCF (Figure 1b), reaching a maximum of 1.70 mg m^{-3} (170 mg m^{-2}). Despite both regions representing significant departures above the background chlorophyll level, the highest chlorophyll concentration was almost twice as strong again at 2.48 mg m^{-3} (282 mg m^{-2}) occurring in a patch centered on 52.25°S (hereafter "the bloom") and confined to the SACCF frontal jet (highlighted by the yellow box in Figures 2–5).

The bloom was located immediately north of the upwelling feature at 52.4°S and had an along-transect width of approximately 35 km, with a small (~6 km wide) patch of lower chlorophyll concentration at its center. Surface nitrate concentration peaked within the upwelling at 28.6 µmol l^{-1} and decreased northward across the bloom reaching 23.7 µmol l^{-1} at its northern edge (Figure 3a). We returned to the location of the bloom after completion of the transect to perform station 6 (indicated in Figures 1–5 by the star), approximately 47 hr after crossing the bloom with the Triaxus. During station 6, net primary productivity (PP) at 20 m depth was measured as 49.2 ± 1.9 mgC $m^{-3}d^{-1}$, a rate as high as has previously been measured in Fe-rich coastal Antarctic waters (Trimborn et al., 2015). Satellite observation of the bloom is severely limited by frequent cloud cover; however, the bloom was visible on the day of station 6 extending approximately 170 km east of the transect (Figure 1c), a distance, which could be covered within 4 days at a nominal speed of 0.5 m s^{-1} within the SACCF jet. A bloom of larger area was visible upstream (approximately centered on 51.5°S, 28°W), though the area between the two regions was obscured.

4.3. Structure Near the Bloom

The entire section of the transect between the PF and SACCF is downstream of the Georgia Basin (Figure 1a); hence, horizontal advection from upstream may provide nutrients and an extant phytoplankton community from

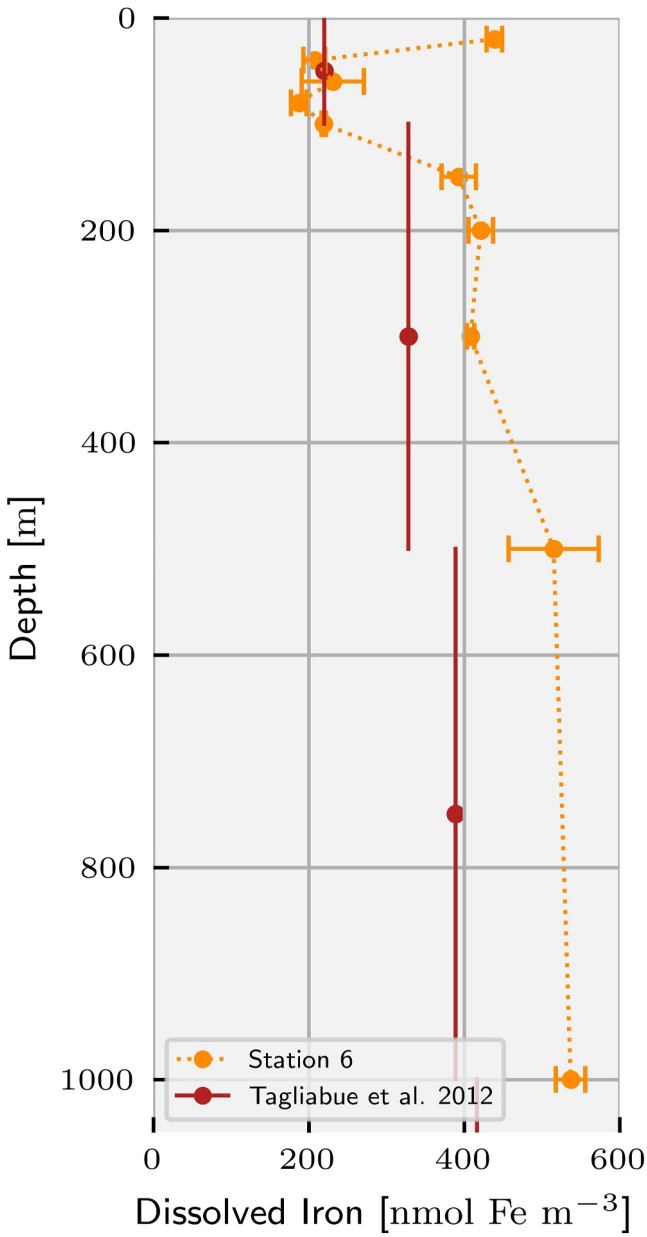

Figure 6. Dissolved iron concentration measured at station 6 (orange), 47 hr after crossing the bloom during the transect. The approximate position of station 6 is indicated with a star in all preceding figures. The median dissolved iron concentration within a given depth range taken from a compilation of measurements made south of the polar front in the Atlantic (Tagliabue et al., 2012) is given in red for context. Vertical bars indicate the range of the depth bin.

upstream. The intense chlorophyll concentrations at the bloom, however, were comparable in strength to coastal waters and were found only in a narrow band within the SACCF frontal jet, which has been proposed to carry benthic sediments and associated iron from the South Georgia shelf (Nielsdóttir et al., 2012) and which may provide a source of new (i.e., not biologically recycled) Fe into the surface from below.

In this region, normalized relative vorticity (≈Ro, Figure 4a) exhibits a pattern of strong meridional gradients extending to 150 m depth in coherent columns across the SACCF and bloom. The large-scale buoyancy change across the SACCF was not observed as a single large step, but was instead a series of lesser buoyancy changes where progressively (northward) lighter isopycnals outcropped across its 35 km wide central portion (Figure 5a). These minor gradients (fronts) appear to have been in approximate thermal wind balance with fluctuations in surface zonal velocity, generating the observed pattern in vorticity and leading to peaks superimposed on the eastward flow (Figure 5c).

4.4. Wind-Driven Processes

Eastward wind stress, taken as a temporal mean over the duration of the transect and 1 week prior, was approximately 0.26 N m^{-2} across the bloom (not shown). This would establish a northward Ekman current, with a depth H_e ≈55 m (Equation 1), and examining the shape of isopycnals near the upwelling in Figure 4 provides evidence of this current. At the southern edge of the upwelling, the outcropping isopycnal curves northward within the mixed layer creating a small "notch" extending approximately 4 km across the higher density, upwelled waters. This notch is consistent with eastward wind stress (up-front on this side of the upwelling) driving lighter water from the south across the upwelling's southern edge. It is reasonable to assume that the equivalent process for down-front winds is also active at the northern edge (52.4°S); however, here, the transport is of dense water over lighter water and would lead to unstable stratification.

The transport of water across fronts is expected to increase potential vorticity (PV) below the Ekman layer where winds are up-front and destroy PV where they are down-front (Thomas, 2005). This modification of PV is evident in Figure 4b where strong PV is evident near 50 m at the southern edge of the upwelling where the eastward winds blow up-front. Conversely, where the eastward winds blow down-front on the northern edge of the upwelling and within the SACCF frontal jet, PV extraction by the winds has resulted in two patches of near-zero PV at the base of the mixed layer. This is consistent with the erosion of the pycnocline below the mixed layer in these patches from a step-like function to a more continuous change in density.

Figure 5b shows the EBF alongside the mean vertical stratification ($\overline{N^2}$) in the upper 150 m, which in all cases includes the mixed layer and the strongly stratified ocean below. Locations where EBF has positive peaks closely match with the locations where mean stratification in the upper 150 m is reduced and where PV at the base of the mixed layer is absent or eroded (e.g., between 52.35°S and 52.45°S, Figure 4b). Positive EBF drives the extraction of buoyancy from below the Ekman layer, which subsequently weakens the gradient across the base of the mixed layer. The reduction of mean stratification in the upper 150 m where EBF peaks suggests that this process has actively eroded the base of the mixed layer within the bloom in two patches across the central portion of the SACCF.

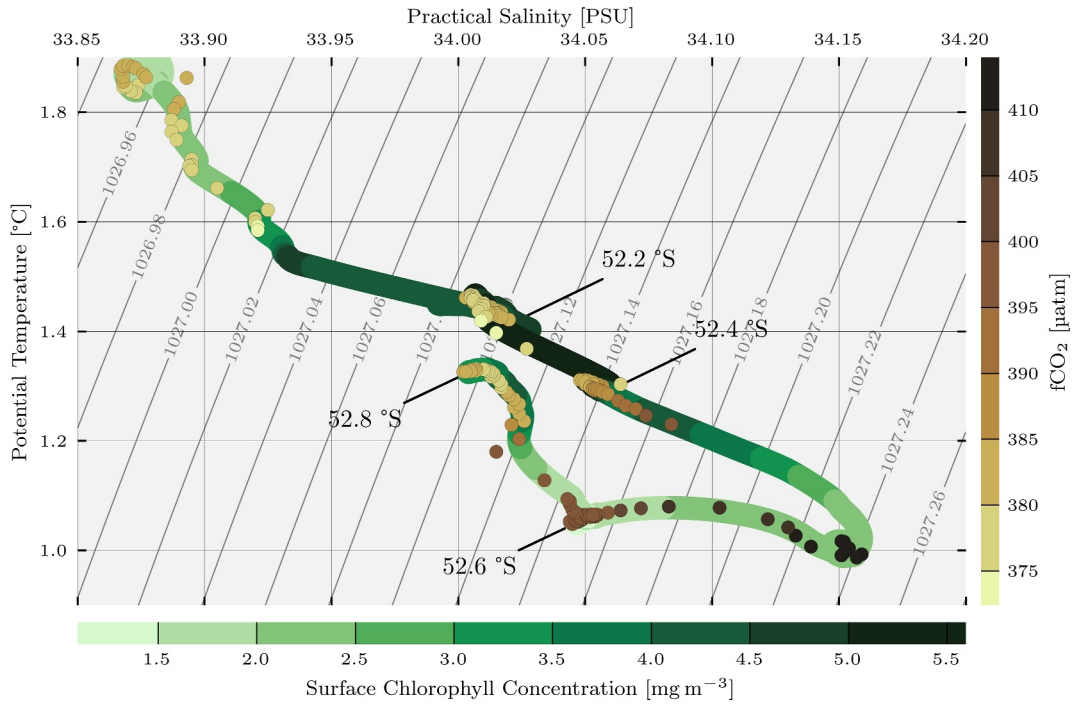

Figure 7. Surface (~11 m depth) temperature and salinity measured by the thermosalinograph, chlorophyll concentration from the FerryBox, and surface fCO_2 calculated from the underway pCO_2 system data. Data are shown between 51.8°S and 52.8°S as in Figures 4 and 5, covering the transit of the bloom and upwelling. Background contours show density in kgm^{-3}. Upwelled dense water (lower right) has $fCO_2 > 410$ µatm and mixes to the north and south, visible as elevated fCO_2 values along the surface mixing lines.

We conclude that the eastward wind stress had modified stratification and PV where horizontal buoyancy gradients exist both at the upwelling location and across much of the SACCF. This occurs largely through the extraction of PV and weakening of the base of the mixed layer by down-front winds blowing across the northern edge of the upwelling, as well as at other more minor density gradients within the SACCF.

4.5. Iron Flux Through Wind-Driven Enhancement of Mixing

Positive EBF eroding stratification and entraining pycnocline water into the mixed layer will subsequently drive a nutrient flux between the layers where there are nutrient gradients between the mixed layer and below. We can estimate the Fe flux potentially driven by EBF-induced enhanced vertical mixing using in situ measurements of Fe concentrations taken near the bloom. The EBF (Figure 5b) represents a flow of buoyancy across the base of the mixed layer, and we can model this as a vertical diffusive process (e.g., Zhuang et al., 2021), such that $EBF \approx \kappa \frac{db}{dz} = \kappa N^2$. Near the northern side of the upwelling where $EBF \approx 2 \times 10^{-7}$ m^2 s^{-3}, we find that $N^2_{max} \approx 2 \times 10^{-5}$ s^{-2} and the vertical diffusion coefficient $\kappa = \frac{EBF}{N^2_{max}} \approx 1 \times 10^{-2}$ m^2 s^{-1} (assuming N^2 is maximum at the base of the mixed layer). By applying the same κ to the Fe gradient across the mixed layer, we can estimate the iron flux as $\mathcal{F}_{Fe} \approx \kappa \frac{\Delta Fe}{\Delta z}$. Trace metal measurements made at station 6 (Figure 6) showed an almost doubling of Fe concentration from 219 nmolFe m^{-3} at 100 m to 393 nmolFe m^{-3} at 150 m, giving a gradient across the base of the mixed layer (~110 m, Figure 2) of 3.5 nmolFe m^{-3} m^{-1}. From this, we calculate a potential iron flux of $\mathcal{F}_{Fe} \approx 3.5 \times 10^{-2}$ nmolFe m^{-2} s^{-1} or ~3 µmolFe m^{-2} d^{-1}. In a 110-m mixed layer, this equates to ~27 nmolFe m^{-3} d^{-1} or ~12% of the existing Fe stock within the mixed layer per day.

While this estimate includes a number of approximations, different approaches give a similar result. McWilliams (2016) gives an approximate scaling for a vertical eddy flux of buoyancy to balance an EBF as $EBF \sim \overline{w'b'}$. Obtaining b' from the threshold density change across the base of the mixed layer (0.05 kg m^{-3}) and calculating the iron flux as $\mathcal{F}_{Fe} \approx w'\Delta Fe$, we arrive at an estimate of ~7 µmolFe m^{-2} d^{-1}. Alternatively, following the calculation of entrainment velocity w_{en} laid out by Whitt, Taylor, and Lévy (2017) considering the deepening of the surface

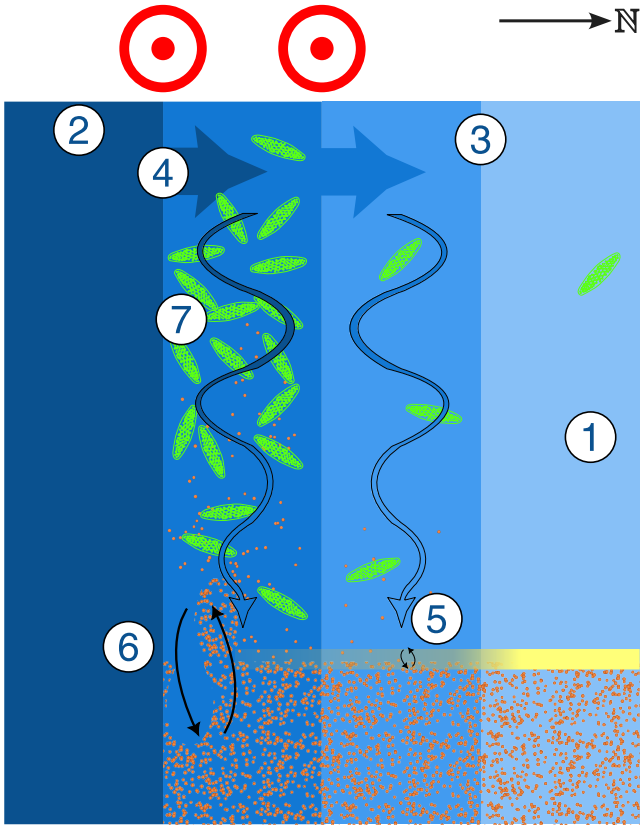

Figure 8. Schematic of the iron supply mechanism driven by Ekman buoyancy flux. In the undisturbed water column (1), an iron-rich layer is separated from the surface by strong stratification (yellow bar); denser (darker blue) surface waters (2) establish a lateral density gradient including sharp fronts (3); transport within the Ekman layer established by down-front (out of the page) winds moves dense water across the front (4), inducing convective mixing, which extracts buoyancy from the layer below; the extraction of buoyancy weakens stratification at the base of the mixed layer (5) and can penetrate the pycnocline (6), entraining deeper, iron-rich waters into the mixed layer and supporting strong phytoplankton growth (7).

mixing layer, we derive an entrainment of ~4 μmolFe m^{-2} d^{-1} (from $w_{en} \approx$ 21 m d^{-1}). It is important to note that our estimate implicitly assumes that the horizontal wind-driven buoyancy flux is converted entirely to a vertical flux across the base of the mixed layer and that this does not allow for a portion of the flux to change the buoyancy of the mixed layer instead. As such, our flux estimate represents a maximum possible value under the observed conditions.

4.6. CO_2 Fugacity and Fluxes

Iron supplied to the surface of the Southern Ocean promotes phytoplankton growth, which can lead to a drawdown of CO_2 from the atmosphere into the ocean. Deeper waters, which are commonly iron-rich also have higher CO_2 concentrations, however, and can release CO_2 to the atmosphere when brought to the surface. In general, the region around the bloom acts as a sink of atmospheric CO_2 (i.e., $\Delta fCO_2 < 0$, Figure 5d). Where waters are not affected by the bloom and upwelling (i.e., north of the yellow box), both ΔfCO_2 and carbon flux are relatively constant at around −14 μatm and –9 mmolC m^{-2} d^{-1}, respectively—typical of the background level between the PF and SACCF (not shown). ΔfCO_2 rises sharply to approximately 13 μatm within the O (10 km) upwelling structure, driving a flux reaching +10 mmolC m^{-2} d^{-1} into the atmosphere. This peak is due to the direct outgassing of CO_2 from the upwelled deep waters, low in oxygen and high in CO_2 and nitrate concentration (compare with Figure 3). ΔfCO_2 south of this feature remains elevated, though it is now negative, reducing the carbon flux to around −2 mmolC m^{-2} d^{-1} along 25 km of the transect. The changes in temperature observed in this subset of the data (location of the black bar in Figure 2a) are small enough to discard the thermal effect as the main driver of fCO_2 variability, leaving the change in the seawater chemistry (due to the upwelling and the biological activity) as the main driver behind the fCO_2 variability.

Carbon flux varies between −10 and −15 mmolC m^{-2} d^{-1} within the phytoplankton bloom north of the upwelling (yellow box, Figure 5d), indicating the absorption of atmospheric CO_2 by the ocean. This is driven by similar changes in fCO_2 due to biological carbon uptake and reaches a maximum amplitude of −20 mmolC m^{-2} d^{-1}. This level of atmospheric carbon drawdown is very similar to the −25.5 mmolC m^{-2} d^{-1} determined by Jones et al. (2017) for the bloom in the Georgia Basin during summertime, closer to South Georgia and much later in the growing season than our observations. The spatial variability of carbon fluxes within the bloom has a similar length scale to the variability in chlorophyll (Figure 5d), EBF (Figure 5b), and surface density gradients (Figure 5a).

5. Discussion

The peaks in chlorophyll concentration encountered along the transect were higher than previous estimates for the South Georgia bloom and both the ACC and Southern Ocean more broadly. Peak concentrations near 51°S and 53°S (1.1 mg m^{-3} and 1.7 mg m^{-3}, respectively) were approximately as strong as the annual maximum concentration of the South Georgia bloom from satellite data (~1.5 mg m^{-3}), calculated as a spatial mean across the typical bloom area (Borrione et al., 2014; Robinson et al., 2016, although both definitions of the typical bloom area include the Georgia Basin but extend no farther than 33°W eastward, excluding our observational area). The vertically integrated standing stocks of chlorophyll near 51°S and 53°S along the transect (124 and 145 mg m^{-2}, respectively) are also greater than almost all of the 117 blooms observed by BGC-Argo floats within the Southern Ocean reported by Ardyna et al. (2019), although their analysis did not include any blooms near South Georgia. Despite this, the chlorophyll concentration at the bloom within the SACCF frontal jet was almost twice as strong again (2.5 mg m^{-3}, 252 mg m^{-2}), exceeding even the 165 mg m^{-2} measured in situ by Hoppe et al. (2017) during summer in the Georgia Basin.

The high chlorophyll concentration in the bloom is remarkable, given that it was far downstream of South Georgia and in early spring when concentrations are unlikely to be at their seasonal maximum. Moreover, the bloom's relative strength along the transect suggests unique environmental conditions concerning the factors, which either promote or limit growth. As our observations were made very early in the South Georgia bloom season (Borrione et al., 2014), grazers are unlikely to be a major controlling factor, and we find it unlikely that there are significant differences in bloom ages. Similarly, given the open ocean location and similar latitude along the transect, differential light availability is also unlikely to explain the observed bloom strength. Instead, the mechanism we have described of iron flux through wind-driven enhanced vertical mixing allows for an ongoing exchange between the surface and a potentially iron-enriched deeper layer, promoting growth at the bloom where horizontal density gradients are strong within the SACCF.

5.1. Comparative Strength of Iron Supply and Demand at the Bloom

In order to assess whether the strength of the iron flux we propose is justified, we can estimate the overall Fe demand of the bloom from the measured net PP at station 6 of 49.2 ± 1.9 mg m^{-3} d^{-1} at 20 m depth. Taking into account that our euphotic depth is ∼50 m, chlorophyll concentration (therefore attenuation) is constant with depth and that PP is linear with incoming light intensity, we calculate vertically integrated PP as 3.3 ± 0.1 g m^{-2} d^{-1} (using the Beer-Lambert law to model its vertical structure as exponential decay from the surface to 1% of its surface value at euphotic depth). We also determined that the in situ community at station 6 took up 4.5 ± 0.7 μmolFe $molC^{-1}$; using this, we can convert integrated PP to a daily Fe demand of 1.2 ± 0.1 μmolFe m^{-2} d^{-1} (assuming no change of Fe:C stoichiometry with depth).

Our estimated Fe demand is ∼4 times greater than that estimated by Schlosser et al. (2018), who performed a similar calculation using assumed values for PP and Fe:C stoichiometry rather than in situ measurements upon which our calculation is based. Most of the discrepancy with our calculated Fe requirement is explained by the PP value they adopt (0.74 ± 0.25 g m^{-2} d^{-1}, derived from remote sensing) being ∼4.5 times lower than that calculated from our measurement at 20 m depth. Conversely, the Fe:C ratio we measured at station 6 fits the Fe:C ratio (5.2 ± 2.8 μmolFe $molC^{-1}$) assumed by Schlosser et al. (2018) well. This ratio was selected to reflect a Southern Ocean community adapted to low Fe concentrations and the calculated Fe demand hence reflected a minimum requirement for a bloom.

We estimated an iron flux between 3 and 7 μmolFe m^{-2} d^{-1} and have reported the first values observed during the spring season. This flux is several orders of magnitude larger than the vertical diffusive flux calculated for the Southern Ocean by Tagliabue et al. (2014) of 0.0157 μmolFe m^{-2} d^{-1}, taking a nominal value of 10^{-4} m^2 s^{-1} for vertical diffusivity. Schine et al. (2021) reported on a bloom linked to hydrothermal vents near the Ross Sea, for which they estimated a flux of 0.44–0.53 μmolFe m^{-2} d^{-1} driven by enhanced vertical mixing through breaking internal waves and which is an order of magnitude lower than our estimations. Our estimate would be among the highest daily iron fluxes collated by Boyd et al. (2012), comparable to fluxes generated by sediment resuspension. The daily iron demand estimated for the bloom, however, justifies the strong flux from the mechanism we propose, assuming no additional input from other strong sources.

Our proposed $\mathcal{F}_{Fe}$ is supported by observations of a strong, shallow ferricline between 100 and 150 m depth in the bloom region with a gradient of 3.5 nmolFe m^{-3} m^{-1}. This slightly exceeds the maximum gradient of 3.2 nmol Fe m^{-3} m^{-1} reported by Schallenberg et al. (2018) at intense bloom sites (chlorophyll concentrations approx. 120 mg m^{-2}) near the SACCF south of the Kerguelen Plateau. Tagliabue et al. (2014) report a similar gradient to ours at the ferricline in the Georgia Basin; however, through associating the ferricline with a deeper isopycnal (27.75 kg m^{-3} compared to 27.24 kg m^{-3} in our study area), they locate it lower in the water column at a depth in excess of 500 m. Consequently, their reported iron gradient at the base of the ML in the Georgia Basin is less than 0.5 nmolFe m^{-3} m^{-1}, leading to the far weaker supply by diapycnal diffusion downstream of South Georgia (estimated as less than 0.3 nmolFE m^{-2} d^{-1}). The authors remark that the vertical iron gradient is strongest within the South Atlantic sector, likely due to "subsurface lateral transfer from numerous regional islands" such as South Georgia, but we observed this gradient far shallower in the water column than expected. We conclude that independent of any enhanced vertical mixing, the strengthened and shallower ferricline alone would elevate Fe supply beyond these typical estimates.

We similarly estimate a significantly enhanced vertical mixing, relative to both typical values for the Southern Ocean (Wu et al., 2011) and an order of magnitude above the enhanced vertical mixing of Schine et al. (2021)

(although the process enhancing mixing differs). We lack estimates of vertical diffusivity based on direct observations of turbulence; however, values of κ_z O(1×10^{-2} m^2 s^{-1}) have been reported previously in the Scotia Sea (Naveira Garabato et al., 2004), albeit deeper in the water column above rough topography. Previous studies (e.g., Schlosser et al., 2018; Tagliabue et al., 2014) tend to estimate an Fe flux based on background levels of diapycnal mixing of O (1×10^{-2} μmolFe m^{-2} d^{-1}), and so the increased vertical diffusivity alone would lead to a heightened Fe flux. Taking, for example, the iron gradient reported by Tagliabue et al. (2014) at the base of the ML in the Georgia Basin would lead to an iron flux of ∼0.4 μmolFe m^{-2} d^{-1} with the enhanced mixing we propose—an order of magnitude below our calculated flux. It is clear that the Fe flux we obtain from our observations is then a result of both strong diapycnal mixing and a strong Fe gradient below the mixed layer.

Our calculations assume that the entirety of the lateral buoyancy flux occurring within the Ekman layer is converted into a vertical flux of buoyancy in the water column below this layer and that this subsequently drives mixing at the base of the mixed layer. The lateral flux could alternatively go toward changing the buoyancy of the mixed layer, leading to no induced vertical mixing across its base. In reality, as long as there is a nonstep change in density at the base of the mixed layer, it is likely that a mixture of the two processes is ongoing with a portion of the flux driving buoyancy change and a portion leading to entrainment. Consequently our flux estimate is likely to be an overestimation, and we present it is an upper limit; however, if only 10% of the EBF were converted to vertical mixing, then the Fe flux would still provide between 25% and 65% of the estimated Fe demand of the bloom. If any more than a negligible fraction of the EBF is successfully converted, then the resulting flux remains a major source of Fe in the open ocean at the bloom.

5.2. Impact and Wider Implications

It is plausible that the iron was supplied directly to the surface layer from the upwelled waters immediately south of the bloom, with no need to invoke any additional processes. Despite upwelled waters mixing into the surface both to the north and the south of the upwelling, it is only north of the upwelling where the intense bloom is triggered (Figure 7, darkest greens). As the environmental conditions (temperature, MLD, and macronutrients) are similar both north and south of the upwelling, we find it unlikely that iron was supplied directly and conclude that the EBF mechanism was necessary to achieve iron supply. Instead, by modifying the density structure across the SACCF, the upwelling generated the iron supply indirectly by creating the conditions appropriate for EBF to generate enhanced vertical mixing. The mechanism, outlined in the schematic given in Figure 8, requires winds blowing along a surface front above a subsurface tracer pool; over time, EBF erodes stratification at the base of the ML and mixing penetrates the tracer pool leading to a vertical tracer flux. Through increasing the strength of the horizontal density gradient, the upwelling increased the strength of the EBF, consequently increasing both the strength and the likelihood of the onset of enhanced mixing between the ML and the tracer pool.

Appropriate wind conditions and horizontal density gradients drive the enhanced vertical mixing, but it is also clear that a strong Fe gradient below the mixed layer is required to establish the significant Fe flux we report. This implies that the flux persists only as long as the gradient is maintained through consumption at the surface and supply below. Supplying an Fe flux into the mixed layer of 3 μmolFe m^{-2} d^{-1} from a deeper layer with a relative Fe excess of 0.2 μmolFe m^{-3} requires the ferricline to descend 15 m per day. This would rapidly deplete the deeper Fe pool and lead to cessation of the flux if it is not resupplied, reducing the impact of the supply to individual events. Consequently, the mechanism we present maybe most applicable in regions downstream of recent strong Fe sources, such as South Georgia and similar islands. In the present case, it is plausible that sediments transported from South Georgia along the SACCF (Nielsdóttir et al., 2012) produce the subsurface pool of iron-rich water and strong ferricline, which is crucial for the Fe flux. These sediments may also help replenish the Fe pool, prolonging the flux duration. As the bloom was downstream of the South Georgia shelf (Figure 1), waters were likely also fertilized with bioavailable iron released either by microbial activity in the low oxygen shelf sediment, or through the remineralization of sediment resuspended into the bottom layers (Borrione et al., 2014). Venables and Meredith (2009) found it likely that iron-rich waters from South Georgia can be transported as far as 20°W below the surface by geostrophic transport. Subsurface transport would protect the available iron from uptake within the euphotic zone, maintaining the iron pool below the mixed layer.

The interplay of the processes upwelling deep waters and supplying iron to the bloom played a controlling role on the variability of chlorophyll and surface carbon fluxes in the local region. While the broader transect acted as a sink for atmospheric CO_2, the upwelling caused localized outgassing and reduced CO_2 uptake. In contrast, the

enhanced bloom fueled by the indirect iron supply significantly increased CO_2 uptake over an area similar to the outgassing, resulting in the impacts of the two mechanisms largely offsetting each other. As such, an assessment of the carbon flux based on satellite observations alone would tend to overestimate uptake in the bloom region. Within the bloom, CO_2 uptake peaked at -19 mmolC m^{-2} d^{-1}, which is comparable to the mean flux of -24 mmolC m^{-2} d^{-1} reported over a month for the Georgia Basin bloom derived by Coggins et al. (2023) from float-based observations. The impact of the iron supply on local carbon dynamics far downstream of the island was therefore substantial, but high-resolution, in situ measurements like ours are essential to capture its full extent.

The vertical transport induced need not be limited to iron, and the conditions required to establish vertical exchange through EBF (Figure 8) are not specific to the South Georgia region so are likely to be met elsewhere. Hence, EBF should be considered an additional pathway for localized vertical exchange wherever strong density gradients, persistent down-front winds, and shallow vertical tracer gradients occur. This maybe particularly true in the Southern Ocean, where winds typically blow eastward and frequently align down-front along the fronts of the ACC, but these conditions may also be satisfied in frontal systems across the globe. As the induced mixing is confined to the base of the mixed layer, EBF maybe especially relevant to euphotic biological processes, as the consumption of nutrients within the mixed layer creates sharp gradients across its base.

Our results provide new context for Southern Ocean blooms, which interact with the strong fronts of the ACC, where intermittent iron supply by favorable wind conditions may contribute to the patchiness or longevity of blooms. Furthermore, a recent study by Moreau et al. (2023) examined a recurring bloom on the less dense side of a front in the Weddell Gyre, attributing it to either the alleviation of light limitation or large-scale upwelling of deep water; our findings, however, suggest that EBF-induced mixing could also help explain the occurrence of blooms such as this. As higher resolution surveys become more commonplace, wider studies of the impact of this process and how it affects nutrients and carbon uptake within the ACC will be possible.

6. Summary and Conclusions

We have identified a physical mechanism explaining the strength of a phytoplankton bloom in the Southern ACC front (SACCF). Our results were obtained ~1,000 km downstream of the island of South Georgia and revealed dense water on the southern flank of the SACCF frontal jet with a strong phytoplankton bloom immediately to its north. The bloom was confined to the central portion of the SACCF and had an integrated chlorophyll concentration greater than 250 mg m^{-2}. Eastward wind stress resulted in a northward transport of dense water across surface fronts. This Ekman buoyancy flux (EBF) destabilized the water column and weakened stratification at the base of the mixed layer in two patches, each extending less than 15 km meridionally along the transect. We estimate that the EBF led to enhanced vertical mixing of $O(\sim 1 \times 10^{-2}\ ms^{-2})$ in these patches, ultimately driving an iron flux from below the mixed layer into the bloom with an upper limit ~3 μmolFe m^{-2} d^{-1}. This flux is of the same order of magnitude as the daily iron utilization of the bloom, estimated from in situ observation as ~1.2 μmolFe m^{-2} d^{-1}, which led to the daily drawdown of atmospheric carbon of ~10 mmolC m^{-2} d^{-1}.

Our observations were crucially dependent on the horizontal resolution achieved with the towed undulating Triaxus. The patches of high EBF and reduced stratification had a total along-transect (cross-flow) extent of less than 30 km. This phenomenon occurred in a SACCF meander with a zonal extent of ~110 km. Assuming that this is the along-flow extent of the patches, this results in an approximate area of 3,300 km^2, or about 2% of the areal extent of the bloom in the Georgia Basin, which is upstream of the part of the ACC considered here. Strong surface density gradients, down-front winds, and vertical tracer gradients across the base of the mixed layer are the key components required for EBF to act and supply significant amounts of iron to the euphotic layer. These requirements are likely fulfilled in other locations of the ACC. Hence, similar dynamics probably also take place in, for example, the blooms associated with the Kerguelen and Crozet islands.

We have shown how iron can be brought to the surface of the open ocean from deeper layers, but the link between the bloom we observed and the assumed South Georgia shelf source of high iron concentrations in the subsurface waters is not yet clear. Tracking particles in a Lagrangian sense might elucidate subsurface pathways along which bioavailable iron travels downstream from island injection sites such as the South Georgia shelf to bloom areas far downstream. Biogeochemical processes may modify iron concentrations along the pathways, and hence, they need also to be considered in order to determine how the subsurface iron pool is maintained. Any seasonality in EBF would also likely impact the annual iron budget and bloom strength in the South Georgia system. Given the

limited temporal coverage of the observations presented here, comparable observations in a similar location are required at other times, specifically later in the growing season. Such observations might improve our understanding of the dynamics of iron stocks within the subsurface iron pool, as well as how the EBF mediated iron supply changes as the mixed layer depth varies throughout the season.

We conclude that wind-driven vertical exchange at frontal boundaries, although previously unrecognized, could be a key mechanism that supplies Southern Ocean blooms with sufficient iron. However, future work remains to constrain its spatial prominence and how it might change in the future. Given the global significance of Southern Ocean blooms for biological carbon drawdown from the atmosphere, we expect that this mechanism might amplify any impacts of changing wind patterns on future CO_2 fluxes.

Conflict of Interest

The authors declare no conflicts of interest relevant to this study.

Data Availability Statement

Triaxus data used in this study are available on Pangaea at von Appen et al. (2023). vmADCP data used in this study are available on Zenodo at Mole et al. (2025). The thermosalinograph data used in this study are available on Pangaea at Hoppmann et al. (2023). Station 6 data, including the vertical iron profile, iron uptake, and primary production are available at Stimpfle et al. (2025). This study has been conducted using E.U. Copernicus Marine Service Information: https://doi.org/10.48670/moi-00149 and https://doi.org/10.48670/moi-00305 for sea surface height and wind data, respectively. Bathymetry data were obtained from GEBCO Compilation Group (2022) GEBCO 2022 Grid (https://doi.org/10.5285/e0f0bb80-ab44-2739-e053-6c86abc0289c).

Acknowledgments

We thank the captain and crew of the RV *Polarstern* and the cruise leader for their efforts and support throughout the *Island Impacts* research cruise *PS133.1*, in face of the unique challenges brought about by working in the open Southern Ocean during inhospitable times of the year. We also thank in particular Jens Hölemann, Annika Oetjens, and Anna Hölemann for their work at sea and dedication to keep the Triaxus continuously deployed. Lilian Dove is appreciated for helpful discussion and provision of data during the cruise. Finally, we also thank Christine Klass, Dieter Wolf-Gladrow, Leticia Cotrim da Cunha, and Rodrigo Kerr as well as the anonymous reviewers for helpful comments and improvements to the manuscript. Ship time was provided by Grant AWI_PS133/1_02, AWI_PS133/1_04, and AWI_PS133/1_05 of the RV *Polarstern*. A. Piñango acknowledges his doctoral scholarship from the Brazilian Federal Agency for Support and Evaluation of Graduate Education (CAPES), process No. 88887.655459/2021-00. Open Access funding enabled and organized by Projekt DEAL.

References

Ardyna, M., Lacour, L., Sergi, S., d'Ovidio, F., Sallée, J.-B., Rembauville, M., et al. (2019). Hydrothermal vents trigger massive phytoplankton blooms in the Southern Ocean. *Nature Communications*, *10*(1), 2451. https://doi.org/10.1038/s41467-019-09973-6

Bachman, S. D., & Klocker, A. (2020). Interaction of jets and submesoscale dynamics leads to rapid ocean ventilation. *Journal of Physical Oceanography*, *50*(10), 2873–2883. https://doi.org/10.1175/JPO-D-20-0117.1

Balaguer, J., Koch, F., Flintrop, C. M., Völkner, C., Iversen, M. H., & Trimborn, S. (2023). Iron and manganese availability drives primary production and carbon export in the Weddell Sea. *Current Biology*, *33*(20), 4405–4414.e4. https://doi.org/10.1016/j.cub.2023.08.086

Böckmann, S., Koch, F., Meyer, B., Pausch, F., Iversen, M., Driscoll, R., et al. (2021). Salp fecal pellets release more bioavailable iron to Southern Ocean phytoplankton than krill fecal pellets. *Current Biology*, *31*(13), 2737–2746.e3. https://doi.org/10.1016/j.cub.2021.02.033

Borrione, I., Aumont, O., Nielsdóttir, M. C., & Schlitzer, R. (2014). Sedimentary and atmospheric sources of iron around South Georgia, Southern Ocean: A modelling perspective. *Biogeosciences*, *11*(7), 1981–2001. https://doi.org/10.5194/bg-11-1981-2014

Boyd, P. W., Arrigo, K. R., Strzepek, R., & van Dijken, G. L. (2012). Mapping phytoplankton iron utilization: Insights into Southern Ocean supply mechanisms. *Journal of Geophysical Research*, *117*(C6). https://doi.org/10.1029/2011JC007726

Boyd, P. W., Jickells, T., Law, C. S., Blain, S., Boyle, E. A., Buesseler, K. O., et al. (2007). Mesoscale iron enrichment experiments 1993-2005: Synthesis and future directions. *Science*, *315*(5812), 612–617. https://doi.org/10.1126/science.1131669

Bushinsky, S. M., Landschützer, P., Rödenbeck, C., Gray, A. R., Baker, D., Mazloff, M. R., et al. (2019). Reassessing Southern Ocean air-sea CO_2 flux estimates with the addition of biogeochemical float observations. *Global Biogeochemical Cycles*, *33*(11), 1370–1388. https://doi.org/10.1029/2019GB006176

Coggins, A., Watson, A. J., Schuster, U., Mackay, N., King, B., McDonagh, E., & Poulton, A. J. (2023). Surface ocean carbon budget in the 2017 South Georgia diatom bloom: Observations and validation of profiling biogeochemical Argo floats. *Deep Sea Research Part II: Topical Studies in Oceanography*, *209*, 105275. https://doi.org/10.1016/j.dsr2.2023.105275

Cutter, G., Casciotti, K., Croot, P., Geibert, W., Heimbürger, L.-E., Lohan, M., et al. (2017). *Sampling and Sample-handling protocols for GEOTRACES cruises. Version 3, August 2017*. [Report]. GEOTRACES International Project Office. https://doi.org/10.25607/OBP-2

de Baar, H. J. W., de Jong, J. T. M., Bakker, D. C. E., Löscher, B. M., Veth, C., Bathmann, U., & Smetacek, V. (1995). Importance of iron for plankton blooms and carbon dioxide drawdown in the Southern Ocean. *Nature*, *373*(6513), 412–415. https://doi.org/10.1038/373412a0

de Jong, J., Schoemann, V., Lannuzel, D., Croot, P., de Baar, H., & Tison, J.-L. (2012). Natural iron fertilization of the Atlantic sector of the Southern Ocean by continental shelf sources of the Antarctic Peninsula. *Journal of Geophysical Research*, *117*(G1). https://doi.org/10.1029/2011JG001679

Dickson, A. G., Sabine, C. L., & Christian, J. R. (2007). *Guide to best practices for ocean CO_2 measurements*. North Pacific Marine Science Organization. https://doi.org/10.25607/OBP-1342

Graham, R. M., De Boer, A. M., van Sebille, E., Kohfeld, K. E., & Schlosser, C. (2015). Inferring source regions and supply mechanisms of iron in the Southern Ocean from satellite chlorophyll data. *Deep Sea Research Part I: Oceanographic Research Papers*, *104*, 9–25. https://doi.org/10.1016/j.dsr.2015.05.007

Gruber, N., Landschützer, P., & Lovenduski, N. S. (2019). The variable Southern Ocean carbon sink. *Annual Review of Marine Science*, *11*(1), 159–186. https://doi.org/10.1146/annurev-marine-121916-063407

Hoppe, C., Klaas, C., Ossebaar, S., Soppa, M., Cheah, W., Laglera, L., et al. (2017). Controls of primary production in two phytoplankton blooms in the Antarctic circumpolar current. *Deep Sea Research Part II: Topical Studies in Oceanography*, *138*, 63–73. https://doi.org/10.1016/j.dsr2.2015.10.005

Hoppmann, M., Tippenhauer, S., & Klaas, C. (2023). Continuous thermosalinograph oceanography along RV POLARSTERN cruise track PS133/1 [Dataset]. *PANGAEA*. https://doi.org/10.1594/PANGAEA.964287

Jones, E. M., Bakker, D. C. E., Venables, H. J., & Watson, A. J. (2012). Dynamic seasonal cycling of inorganic carbon downstream of South Georgia, Southern Ocean. *Deep Sea Research Part II: Topical Studies in Oceanography*, *59–60*, 25–35. https://doi.org/10.1016/j.dsr2.2011.08.001

Jones, E. M., Hoppema, M., Strass, V., Hauck, J., Salt, L., Ossebaar, S., et al. (2017). Mesoscale features create hotspots of carbon uptake in the Antarctic Circumpolar current. *Deep Sea Research Part II: Topical Studies in Oceanography*, *138*, 39–51. https://doi.org/10.1016/j.dsr2.2015.10.006

Klocker, A. (2018). Opening the window to the Southern Ocean: The role of jet dynamics. *Science Advances*, *4*(10), eaao4719. https://doi.org/10.1126/sciadv.aao4719

Korb, R. E., Whitehouse, M. J., Atkinson, A., & Thorpe, S. E. (2008). Magnitude and maintenance of the phytoplankton bloom at South Georgia: A naturally iron-replete environment. *Marine Ecology Progress Series*, *368*, 75–91. https://doi.org/10.3354/meps07525

Korb, R. E., Whitehouse, M. J., & Ward, P. (2004). SeaWiFS in the Southern Ocean: Spatial and temporal variability in phytoplankton biomass around South Georgia. *Deep Sea Research Part II: Topical Studies in Oceanography*, *51*(1), 99–116. https://doi.org/10.1016/j.dsr2.2003.04.002

Martin, J. H., Fitzwater, S. E., & Gordon, R. M. (1990). Iron deficiency limits phytoplankton growth in Antarctic waters. *Global Biogeochemical Cycles*, *4*(1), 5–12. https://doi.org/10.1029/GB004i001p00005

McWilliams, J. C. (2016). Submesoscale currents in the ocean. *Proceedings of the Royal Society A: Mathematical, Physical and Engineering Sciences*, *472*(2189), 20160117. https://doi.org/10.1098/rspa.2016.0117

Meredith, M. P., Meijers, A. S., Naveira Garabato, A. C., Brown, P. J., Venables, H. J., Abrahamsen, E. P., et al. (2015). Circulation, retention, and mixing of waters within the Weddell-scotia confluence, Southern Ocean: The role of stratified Taylor columns. *Journal of Geophysical Research: Oceans*, *120*(1), 547–562. https://doi.org/10.1002/2014JC010462

Mole, R., von Appen, W.-J., Hoelemann, J., Oetjens, A., Hoelemann, A., & Becker, H. (2025). Vessel-mounted ADCP ocean velocity data across a section of the Antarctic circumpolar current—RV polarstern PS133/1 (Oct 2022) [Dataset]. *Zenodo*. https://doi.org/10.5281/zenodo.16313593

Moreau, S., Hattermann, T., de Steur, L., Kauko, H. M., Ahonen, H., Ardelan, M., et al. (2023). Wind-driven upwelling of iron sustains dense blooms and food webs in the eastern Weddell Gyre. *Nature Communications*, *14*(1), 1303. https://doi.org/10.1038/s41467-023-36992-1

Naveira Garabato, A. C. N., Polzin, K. L., King, B. A., Heywood, K. J., & Visbeck, M. (2004). Widespread intense turbulent mixing in the Southern Ocean. *Science*, *303*(5655), 210–213. https://doi.org/10.1126/science.1090929

Nicholson, S.-A., Lévy, M., Jouanno, J., Capet, X., Swart, S., & Monteiro, P. M. S. (2019). Iron supply pathways between the surface and subsurface waters of the Southern Ocean: From winter entrainment to summer storms. *Geophysical Research Letters*, *46*(24), 14567–14575. https://doi.org/10.1029/2019GL084657

Nielsdóttir, M. C., Bibby, T. S., Moore, C. M., Hinz, D. J., Sanders, R., Whitehouse, M., et al. (2012). Seasonal and spatial dynamics of iron availability in the scotia sea. *Marine Chemistry*, *130–131*, 62–72. https://doi.org/10.1016/j.marchem.2011.12.004

Petersen, W. (2014). FerryBox systems: State-of-the-art in Europe and future development. *Journal of Marine Systems*, *140*, 4–12. https://doi.org/10.1016/j.jmarsys.2014.07.003

Reagan, J. R., Boyer, T. P., García, H. E., Locarnini, R. A., Baranova, O. K., Bouchard, C., et al. (2024). *World ocean atlas 2023*. NOAA National Centers for Environmental Information.

Rintoul, S. R. (2018). The global influence of localized dynamics in the Southern Ocean. *Nature*, *558*(7709), 209–218. https://doi.org/10.1038/s41586-018-0182-3

Robinson, J., Popova, E. E., Srokosz, M. A., & Yool, A. (2016). A tale of three islands: Downstream natural iron fertilization in the Southern Ocean. *Journal of Geophysical Research: Oceans*, *121*(5), 3350–3371. https://doi.org/10.1002/2015JC011319

Schallenberg, C., Bestley, S., Klocker, A., Trull, T. W., Davies, D. M., Gault-Ringold, M., et al. (2018). Sustained upwelling of subsurface iron supplies seasonally persistent phytoplankton blooms around the Southern Kerguelen Plateau, Southern Ocean. *Journal of Geophysical Research: Oceans*, *123*(8), 5986–6003. https://doi.org/10.1029/2018JC013932

Schine, C. M. S., Alderkamp, A.-C., van Dijken, G., Gerringa, L. J. A., Sergi, S., Laan, P., et al. (2021). Massive Southern Ocean phytoplankton bloom fed by iron of possible hydrothermal origin. *Nature Communications*, *12*(1), 1211. https://doi.org/10.1038/s41467-021-21339-5

Schlosser, C., Schmidt, K., Aquilina, A., Homoky, W. B., Castrillejo, M., Mills, R. A., et al. (2018). Mechanisms of dissolved and labile particulate iron supply to shelf waters and phytoplankton blooms off South Georgia, Southern Ocean. *Biogeosciences*, *15*(16), 4973–4993. https://doi.org/10.5194/bg-15-4973-2018

Sergi, S., Baudena, A., Cotté, C., Ardyna, M., Blain, S., & d'Ovidio, F. (2020). Interaction of the Antarctic circumpolar current with seamounts fuels moderate blooms but vast foraging grounds for multiple marine predators. *Frontiers in Marine Science*, *7*. https://doi.org/10.3389/fmars.2020.00416

Stimpfle, J., Voelkner, C., Ebner, B., Stimac, I., Bussmann, F., Terbrueggen, A., & Trimborn, S. (2025). PS133.1_6 dissolved iron profile; surface primary production and iron uptake [Dataset]. *Zenodo*. https://doi.org/10.5281/zenodo.15790326

Strass, V. H., Garabato, A. C. N., Bracher, A. U., Pollard, R. T., & Lucas, M. I. (2002). A 3-D mesoscale map of primary production at the Antarctic polar front: Results of a diagnostic model. *Deep Sea Research Part II: Topical Studies in Oceanography*, *49*(18), 3813–3834. https://doi.org/10.1016/S0967-0645(02)00112-1

Strass, V. H., Leach, H., Prandke, H., Donnelly, M., Bracher, A. U., & Wolf-Gladrow, D. A. (2017). The physical environmental conditions for biogeochemical differences along the Antarctic circumpolar current in the Atlantic sector during late Austral summer 2012. *Deep Sea Research Part II: Topical Studies in Oceanography*, *138*, 6–25. https://doi.org/10.1016/j.dsr2.2016.05.018

Tagliabue, A., Mtshali, T., Aumont, O., Bowie, A. R., Klunder, M. B., Roychoudhury, A. N., & Swart, S. (2012). A global compilation of dissolved iron measurements: Focus on distributions and processes in the Southern Ocean. *Biogeosciences*, *9*(6), 2333–2349. https://doi.org/10.5194/bg-9-2333-2012

Tagliabue, A., Sallée, J.-B., Bowie, A. R., Lévy, M., Swart, S., & Boyd, P. W. (2014). Surface-water iron supplies in the Southern Ocean sustained by deep winter mixing. *Nature Geoscience*, *7*(4), 314–320. https://doi.org/10.1038/ngeo2101

Thomalla, S. J., Nicholson, S.-A., Ryan-Keogh, T. J., & Smith, M. E. (2023). Widespread changes in Southern Ocean phytoplankton blooms linked to climate drivers. *Nature Climate Change*, *13*(9), 975–984. https://doi.org/10.1038/s41558-023-01768-4

Thomas, L., & Ferrari, R. (2008). Friction, frontogenesis, and the stratification of the surface mixed layer. *Journal of Physical Oceanography*, *38*(11), 2501–2518. https://doi.org/10.1175/2008JPO3797.1

Thomas, L. N. (2005). Destruction of potential vorticity by winds. *Journal of Physical Oceanography*, *35*(12), 2457–2466. https://doi.org/10.1175/JPO2830.1

Thomas, L. N., & Lee, C. M. (2005). Intensification of ocean fronts by down-front winds. *Journal of Physical Oceanography*, *35*(6), 1086–1102. https://doi.org/10.1175/JPO2737.1

Trimborn, S., Hoppe, C. J. M., Taylor, B. B., Bracher, A., & Hassler, C. (2015). Physiological characteristics of Open Ocean and coastal phytoplankton communities of Western Antarctic Peninsula and Drake Passage waters. *Deep Sea Research Part I: Oceanographic Research Papers*, *98*, 115–124. https://doi.org/10.1016/j.dsr.2014.12.010

Venables, H., & Moore, C. M. (2010). Phytoplankton and light limitation in the Southern Ocean: Learning from high-nutrient, high-chlorophyll areas. *Journal of Geophysical Research*, *115*(C2), C02015. https://doi.org/10.1029/2009JC005361

Venables, H. J., & Meredith, M. P. (2009). Theory and observations of Ekman flux in the chlorophyll distribution downstream of South Georgia. *Geophysical Research Letters*, *36*(23), 5. https://doi.org/10.1029/2009GL041371

von Appen, W.-J., Hölemann, J. A., Mole, R., Oetjens, A., Hölemann, A., Becker, H., et al. (2023). Raw data from Triaxus topAWI (towed ocean profiler of the AWI) during RV POLARSTERN cruise PS133/1 [Dataset]. *PANGAEA*. https://doi.org/10.1594/PANGAEA.962675

von Appen, W.-J., Strass, V. H., Bracher, A., Xi, H., Hörstmann, C., Iversen, M. H., & Waite, A. M. (2020). High-resolution physical–biogeochemical structure of a filament and an eddy of upwelled water off Northwest Africa. *Ocean Science*, *16*(1), 253–270. https://doi.org/10.5194/os-16-253-2020

Wanninkhof, R. (2014). Relationship between wind speed and gas exchange over the ocean revisited. *Limnology and Oceanography: Methods*, *12*(6), 351–362. https://doi.org/10.4319/lom.2014.12.351

Weiss, R. F. (1974). Carbon dioxide in water and seawater: The solubility of a non-ideal gas. *Marine Chemistry*, *2*(3), 203–215. https://doi.org/10.1016/0304-4203(74)90015-2

Whitt, D. B., Lévy, M., & Taylor, J. R. (2017). Low-frequency and high-frequency oscillatory winds synergistically enhance nutrient entrainment and phytoplankton at fronts. *Journal of Geophysical Research: Oceans*, *122*(2), 1016–1041. https://doi.org/10.1002/2016JC012400

Whitt, D. B., Taylor, J. R., & Lévy, M. (2017). Synoptic-to-planetary scale wind variability enhances phytoplankton biomass at ocean fronts. *Journal of Geophysical Research: Oceans*, *122*(6), 4602–4633. https://doi.org/10.1002/2016JC011899

Wu, L., Jing, Z., Riser, S., & Visbeck, M. (2011). Seasonal and spatial variations of Southern Ocean diapycnal mixing from Argo profiling floats. *Nature Geoscience*, *4*(6), 363–366. https://doi.org/10.1038/ngeo1156

Zhang, Z., Qiu, B., Klein, P., & Travis, S. (2019). The influence of geostrophic strain on Oceanic ageostrophic motion and surface chlorophyll. *Nature Communications*, *10*(1), 2838. https://doi.org/10.1038/s41467-019-10883-w

Zhuang, Z., Yuan, Y., Zheng, Q., Zhou, C., Zhao, X., & Zhang, T. (2021). Effects of buoyancy flux on upper-ocean turbulent mixing generated by non-breaking surface waves observed in the South China Sea. *Journal of Geophysical Research: Oceans*, *126*(5), e2020JC016816. https://doi.org/10.1029/2020JC016816